

Learning a generalized multiscale prolongation operator

YUCHENG LIU¹, SHUBIN FU², YINGJIE ZHOU¹, CHANGQING YE¹, AND
ERIC T. CHUNG¹

¹Department of Mathematics, The Chinese University of Hong Kong, Shatin,
Hong Kong SAR, China.

²Eastern Institute for Advanced Study, Ningbo, China.

Abstract

In this research, we address Darcy flow problems with random permeability using iterative solvers, enhanced by a two-grid preconditioner based on a generalized multiscale prolongation operator, which has been demonstrated to be stable for high contrast profiles. To circumvent the need for repeatedly solving spectral problems with varying coefficients, we harness deep learning techniques to expedite the construction of the generalized multiscale prolongation operator. Considering linear transformations on multiscale basis have no impact on the performance of the preconditioner, we devise a loss function by the coefficient-based distance between subspaces instead of the plain l^2 -norm of the difference of the corresponding multiscale bases. We discover that leveraging the inherent symmetry in the local spectral problem can effectively accelerate the neural network training process. In scenarios where training data are limited, we utilize the Karhunen–Loève expansion to augment the dataset. Extensive numerical experiments with various types of random coefficient models are exhibited, showing that the proposed method can significantly reduce the time required to generate the prolongation operator while maintaining the original efficiency of the two-grid preconditioner. Notably, the neural network demonstrates strong generalization capabilities, as evidenced by its satisfactory performance on unseen random permeability fields.

Keywords: two-grid preconditioner, multiscale bases, Karhunen-Loève expansion, U-Net

MSC codes: 65F08, 65N55, 68T07

1 Introduction

Simulating subsurface fluid flow in heterogeneous porous media is frequently encountered in real-world applications, including reservoir simulation, groundwater resource management, groundwater contamination predictions, and the exploration of oil and gas fields [5, 14]. The properties of a heterogeneous porous medium can vary significantly across different spatial regions and exhibit complex structures, making it essential to carefully account for heterogeneity in simulations [36]. These detailed models result in large linear systems, which in turn lead to computational challenges.

Model reduction techniques, such as upscaling based on homogenization [10, 15, 31, 15, 4], have been rapidly developed. Upscaling is an averaging process that scales the static properties of a fine-grid model to equivalent characteristics at a coarse-grid level. This process aims to ensure that the coarse and fine models share a similar formulation. However, it often fails to capture all the small-scale details of the quantities of interest. Another approach is multiscale model reduction [12], which include the multiscale finite element method [19], the mixed multiscale finite element method [11, 1], the multiscale finite volume method [25, 18], the multiscale mortar mixed finite element method [3] and the generalized multiscale finite element method [16, 13]. The main idea behind these methods is to reduce the problem defined on fine grids to one on coarse grids. The multiscale basis functions encapsulate the heterogeneity of the original geological medium and are defined by solving a series of carefully designed local problems on each coarse grid element. While these

multiscale methods have been successfully applied to various multiscale models, some of the effectiveness can diminish with increasing contrast in permeability and correlation length. When highly precise fine-scale solutions are required, it becomes essential to design an efficient solver that can directly handle the original fine-scale information, rather than relying solely on multiscale methods. Multigrid [8] is one of the most efficient and commonly used algorithms for solving large-scale linear systems [2]. The smoother and the connection (prolongation operator) between different levels are therefore crucial components. The mathematical theory shows that the optimal prolongation operator is defined on eigenvalue problems for fixed smoothing operation [32]. We focus on utilizing neural networks to learn such an optimal prolongation operator.

With the rapid advancement of deep learning, it has become a research hotspot for the numerical solution of differential equations in recent years. Numerous methods have been proposed to apply deep learning directly to solving PDEs. A notable development in this area is the introduction of physics-informed neural networks (PINNs) [24], which have gained significant attention. However, PINNs are limited in their applicability as they learn the solution for a single problem instance. Another popular research area is operator learning [23, 9, 22], which demonstrates improved generalization abilities by focusing on the differential operators rather than one solution determined by the PDEs, initial value conditions and boundary conditions. Compared to traditional algorithms for solving PDEs, neural network-based methods are highly demanding for training data and significant computational resource and have unresolved issues with numerical accuracy and stability. For the interplay between multiscale methods and neural networks, we name a few: a deep learning strategy is proposed to determine multiscale basis functions and coarse-scale parameters for non-static coefficients in [29]; a new deep neural networks approach tailored for model reduction in multiscale porous media flow problems has been developed in [30]. Attention has also been paid to combine learning technique with traditional linear solvers: geometric multigrid methods have been advanced through the application of evolutionary computation for optimizing their techniques [28] and the deep learning approaches for tuning prolongation and restriction operators in two-grid algorithms [20, 17]; graph based neural networks have been adapted to algebraic multigrid methods, enabling the performance on unstructured problems [26].

In this study, we explore the application of neural networks in simulating Darcy flow, focusing specifically on the prolongation operator related to generalized multiscale basis functions derived from the coefficient. We design our neural networks architecture with convolutional layers complemented by upsampling and downsampling layers, which significantly streamline computational and spatial complexities. We have found that exploiting the inherent symmetry in local spectral problems (LSPs) can substantially expedite the training of our neural networks. When faced with limited training data, the Karhunen–Loève expansion proves effective for data augmentation purposes. Linear transformations on generalized multiscale basis do not affect the performance of the preconditioner; therefore, we propose using the coefficient-based distance between subspaces as our loss function instead of l^2 -norm of the difference of the corresponding generalized multiscale basis and provide a theoretical proof to demonstrate its efficacy. Ultimately, our approach enables the direct computation of the prolongation operator, thus obviating the need for the previously complex method of training individual neural networks for each basis function. We underscore that the operators derived via our proposed data-driven deep learning approach exhibit universality, applicable across diverse boundary conditions, transcending the constraints of singular problem environments. Moreover, we test the generalization ability of neural networks which is sufficiently strong to be applicable to permeability profiles from unseen datasets and coarse elements of varying resolutions.

The rest of this paper is organized as follows. Section 2 introduces the model, discretization, and the iterative solver. Section 3 details the deep learning method, defines our loss function by coefficient-based distance between subspaces, proves its efficacy and presents data augmentation methods including inherent symmetry in the LSPs and Karhunen–Loève expansion. Experimental results are showcased in Section 4. Finally, we synthesize the key results and provided outlooks for future research in Section 5.

2 Preliminaries

2.1 Model problem and numerical discretization

We consider the following Darcy flow model of a single-phase fluid in a potentially high-contrast and random medium:

$$\begin{cases} \kappa^{-1} \mathbf{u} + \nabla p = \mathbf{0} & \text{in } \Omega, \\ \nabla \cdot \mathbf{u} = f & \text{in } \Omega, \end{cases} \quad (1)$$

where Ω is the computational domain, κ (scalar-valued random field) is the permeability of the porous medium, \mathbf{u} is the Darcy velocity, p is the pressure field and f is the source term.

For specific numerical discretization, a boundary condition must be established. However, it should be emphasized that our method can be applied for different boundary conditions. Here, we present the numerical discretization under the no-flux boundary condition. Consider the two-point flux approximation (TPFA) to discrete Eq. (1). Let \mathcal{T}^h be a quadrilaterals partition of the computational domain Ω with mesh size h_x in x-direction and h_y in y-direction, N is the number of the element in mesh, \mathcal{E}^h is the set of the internal edges of mesh. By applying mixed finite element method (the lowest-order polynomial finite spaces W_h and the lowest-order Raviart-Thomas finite element space \mathbf{V}_h [7]) with velocity elimination technique [35] and the trapezoidal quadrature rule, we achieve

$$\sum_{e \in \mathcal{E}^h} \kappa_e \llbracket p_h \rrbracket_e \llbracket w_h \rrbracket_e \frac{|e|^2}{h_x h_y} = \int_{\Omega} f w_h \, d\mathbf{x}, \quad \forall w_h \in W_h, \quad (2)$$

where $\kappa_e^{-1} = (\kappa_{e,+}^{-1} + \kappa_{e,-}^{-1})/2$, $(\kappa_{e,-}, \kappa_{e,+})$ is a neighbor pair of an edge $e \in \mathcal{E}^h$, $|e|$ is the length of the edge e and $\llbracket p_h \rrbracket_e, \llbracket w_h \rrbracket_e$ are the jump of element-wisely constant functions p_h, w_h across edge e towards the positive direction.

We can express Eq. (2) as a linear system of equations:

$$AP = F, \quad (3)$$

where $A \in \mathbb{R}^{N \times N}$, $P \in \mathbb{R}^N$ and $F \in \mathbb{R}^N$.

2.2 Two-grid preconditioner

We further elucidated the process of implementing the Preconditioned Conjugate Gradient (PCG) method [33] with the two-grid preconditioner B^{-1} based on generalized multiscale basis to effectively solve the linear system defined in Eq. (3). In the subsequent discussion, we have utilized generalized multiscale space notation to highlight the importance of geometric information, and a notation with “ c ” superscript is associated with the coarse grid. To grasp the key ingredients directly, we introduce several key notations and their specific roles in a two-grid preconditioner:

- R serves as the smoother in fine space W_h .
- B^{-1} acts as a preconditioner of A .
- P is a prolongation operator which links coarse space W_h^c and fine space W_h .
- $B^c = (A^c)^{-1} = (P^T A P)^{-1}$ functions as a solver in coarse space W_h^c .

The two-grid preconditioner can be divided into three main parts: pre-smoothing, coarse grid correction, and post-smoothing. Each stage targets different characteristics of the problem to enhance the overall efficiency and accuracy of the solution. The detailed representation of these phases is shown in Algorithm 1.

Algorithm 1 A two-grid preconditioner B^{-1}

Given right-hand side term r :

- 1: Pre-smoothing: $w \leftarrow Rr$.
 - 2: Coarse grid correction: $w \leftarrow w + PB^cP^\top(r - Aw)$.
 - 3: Post-smoothing: $B^{-1}r \leftarrow w + R(r - Aw)$.
-

2.3 Prolongation operators

Assume the domain Ω is divided into a union of disjoint subdomains denoted by $\{K_j\}_{j=1}^n$ with each K_j consisting of N/n fine elements from \mathcal{T}_h . Denote \mathcal{T}_H as the coarse quadrilaterals partition of the computational domain Ω . The basis functions of finite space W_h restricted to the coarse element K_j form the snapshot space $W_h(K_j)$. Figure 1 is an illustration of the two-scale mesh where τ is a fine element and K_j is a coarse element which contains 16 fine elements.

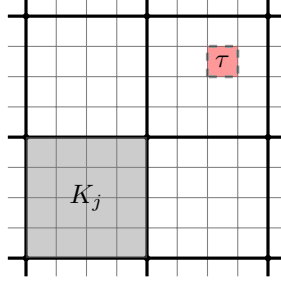


Figure 1: An illustration of the two-scale mesh: τ is a fine element and K_j is a coarse element which contains 16 fine elements.

We introduce the local generalized multiscale basis functions $\{\Phi_{j,k}\}_{k=1}^{n^c}$ associated with the coarse element K_j , where n^c is the number of basis functions on each coarse element. In GMsFEMs [16], two bilinear forms corresponding to the j -th coarse element need to be defined to obtain effective low-dimensional representations from snapshot space $W_h(K_j)$. Here we define

$$\begin{aligned}
 a_j(w'_h, w''_h) &:= \sum_{e \in \mathcal{E}^h(K_j)} \kappa_e \llbracket w'_h \rrbracket_e \llbracket w''_h \rrbracket_e \frac{|e|^2}{h_x h_y}, \quad \forall w'_h, w''_h \in W_h(K_j), \\
 s_j(w'_h, w''_h) &:= \int_{K_j} \tilde{\kappa} w'_h w''_h \, d\mathbf{x}, \quad \forall w'_h, w''_h \in W_h(K_j),
 \end{aligned} \tag{4}$$

where $\mathcal{E}^h(K_j)$ is the internal edge set in the coarse element K_j . It is reasonable to simply set $\tilde{\kappa} = \kappa$, see [35]. The local generalized multiscale basis functions $\{\Phi_{j,k}\}_{k=1}^{n^c}$ is defined by solving the following spectral problem on coarse element K_j :

$$\sum_{e \in \mathcal{E}^h(K_j)} \kappa_e \llbracket \Phi_h \rrbracket_e \llbracket w_h \rrbracket_e \frac{|e|^2}{h_x h_y} = \lambda \int_{K_j} \tilde{\kappa} \Phi_h w_h \, d\mathbf{x}, \quad \forall w_h \in W_h(K_j). \tag{5}$$

Solving the LSP Eq. (5), eigenvectors $\{\Phi_{j,k}\}_{k=1}^{n^c}$ corresponding to the n^c smallest eigenvalues will be the local generalized multiscale basis functions. The direct sum of the basis functions on each coarse element spans the global coarse space and its projection onto the fine space is represented as a prolongation operator P , where each column of P corresponds to a generalized multiscale basis and denote the number of column of P as $N^c = n \times n^c$.

3 Methodology

The coefficient κ is drawn from a random field, indicating that for any κ selected from a specific distribution, multiple spectral problems must be recalculated in order to derive the prolongation operator. The process of solving spectral problems can be viewed as extracting several features of the same size from a coarse element, which is quite similar to panoptic segmentation [21]. Therefore, we aim to propose a neural network architecture that takes a coarse element as input and directly outputs the corresponding part of prolongation operator.

3.1 Neural network architectures

Leveraging the efficiency of the U-Net [27], which excels in panoptic segmentation tasks, we propose multiple level neural networks shown in Fig. 2 specifically designed for spectral problems. In the diagram, the labels along the x-axis represent the number of channels in the corresponding layer, while the labels along the z-axis indicate the dimensions of the image in that layer.

The multiple level neural networks contain consists of the encoder part (contracting path), a bottleneck, the decoder part (expansive path) and a classifier. The specifics include:

- **Convolutional Layers:** Two consecutive convolution processes using a kernel size of 3×3 and padding of 1 are implemented, maintaining the output feature map size unchanged.
- **Pooling Layers:** After the convolutional operations, a max pooling layer with a pool size of 2×2 and a stride of 2 is used to halve the spatial dimensions of the feature maps, providing a form of translation invariance.
- **Upconvolutional Layers:** Initially, a convolution operation with a kernel size of 3×3 , stride of 2, a padding of 1, and output padding of 1 is used to double the spatial dimensions of the feature maps.

The encoder and decoder are directly connected through skip connections. These connections transfer feature maps from the encoder directly to corresponding layers in the decoder, assisting the decoder in better utilizing both high-level features and fine details transferred from the encoder, thereby more accurately reconstructing and localizing the input data.

3.2 Loss function

The prolongation operator P is a block diagonal matrix. Each block is assembled from generalized multiscale basis functions of a coarse element. Since we aim to learn each block of prolongation operator directly, a special distance between two subspaces of $\mathbb{R}^{N/n}$ is proposed based on coefficient κ on a coarse element. In our neural networks, we take $\text{dist}_{\tilde{\kappa}}(\text{target}, \text{prediction})$ as our loss function. Specific definition of the distance is given below.

Definition 1. Denote

$$P_j = [p_{j,1}, p_{j,2}, \dots, p_{j,n^c}], \quad X_j = \text{span}\{p_{j,1}, p_{j,2}, \dots, p_{j,n^c}\},$$

where P_j is a block of prolongation operator based on the j -th coarse element, X_j is a subspace of $\mathbb{R}^{N/n}$ and $\{\psi_{j,1}, \psi_{j,2}, \dots, \psi_{j,n^c}\}$ is an orthonormal basis of subspace X_j with respectively to the inner product $(\cdot, \cdot)_{\tilde{\kappa}}$. These basis functions are arranged column-wise to form the matrix denoted as T_j . For two different prolongation operators $P_j^{(1)}$ and $P_j^{(2)}$, define

$$\text{dist}_{\tilde{\kappa}_j}(P_j^{(1)}, P_j^{(2)}) = \left(n^c - \|(T_j^{(1)})^\top \tilde{\kappa}_j T_j^{(2)}\|_F^2 \right)^{1/2},$$

where $\|\cdot\|_F$ is Frobenius norm and the $\tilde{\kappa}_j$ here is an $N/n \times N/n$ diagonal matrix which is from $\tilde{\kappa}$ restricted on coarse element K_j .

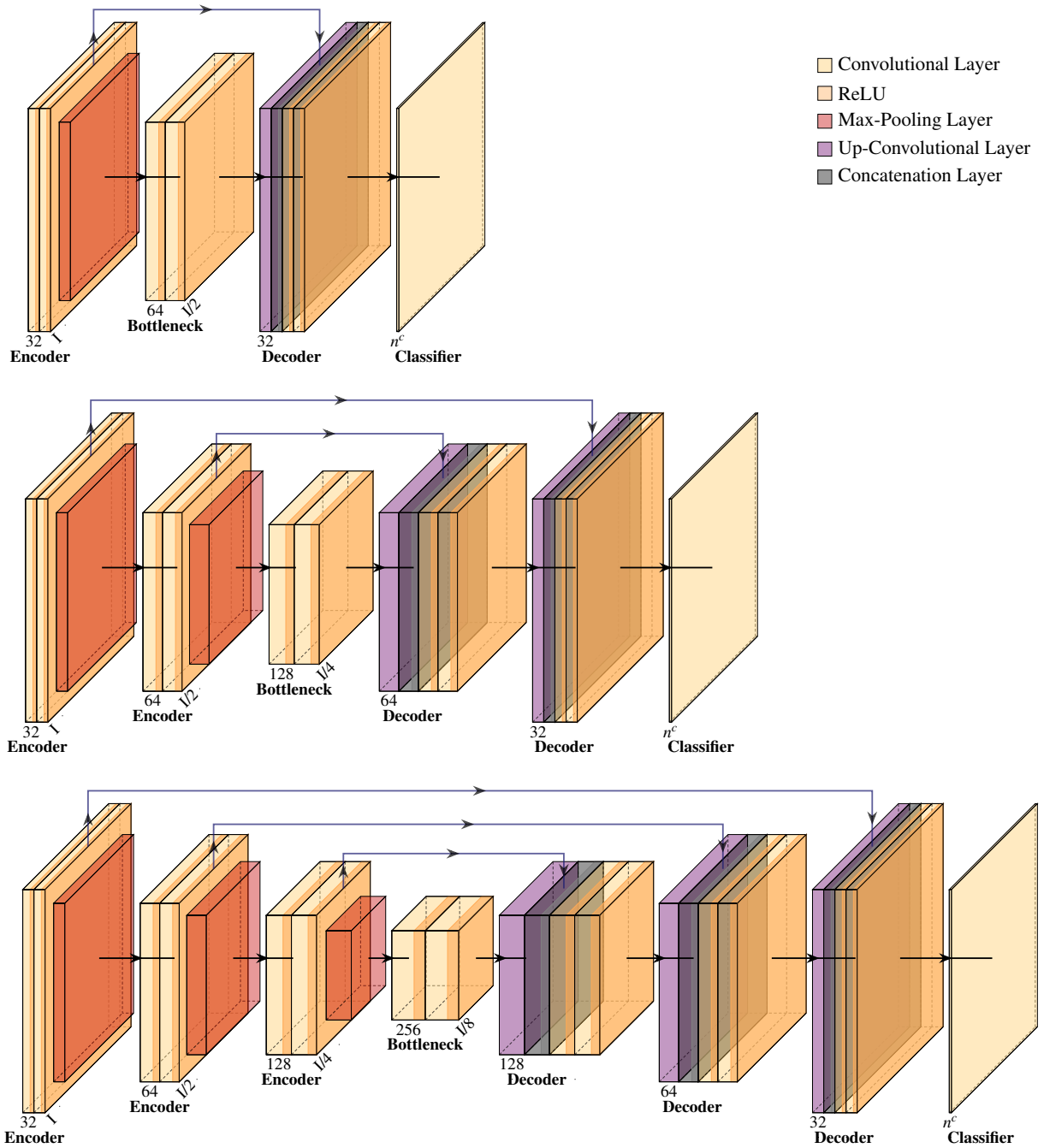


Figure 2: Two-level, three-level and four-level U-Net architectures.

To simplify these expressions, we will omit the index j for the coarse element index in subsequent discussions, whenever it does not lead to ambiguity.

Remark. An intuitive explanation of the above definition of distance in Fig. 3. We first project all the basis vectors in an orthonormal basis of subspace $X^{(2)}$ onto subspace $X^{(1)}$ with respect to $(\cdot, \cdot)_{\tilde{\kappa}}$. The square

of the distance is equal to the sum of the squares of the lengths of residual $A_k B_k$.

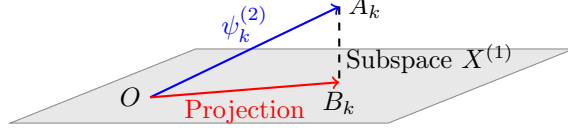


Figure 3: An intuitive diagram of distance defined in the loss function. $\overrightarrow{OA_k}$ is an orthonormal basis of subspace $X^{(2)}$, $\overrightarrow{OB_k}$ is the projection of $\overrightarrow{OA_k}$ onto the subspace $X^{(1)}$ and $\overrightarrow{A_k B_k}$ is the residual of $\overrightarrow{OA_k}$ relative to the subspace $X^{(1)}$.

Next, we need to prove the distance in Definition 1 is well-defined.

Theorem 3.1. *The following properties hold for the distance in Definition 1.*

- *The distance does not depend on the choice of basis.*
- *Non-negativity:* $n^c - \|(T^{(1)})^\top \tilde{\kappa} T^{(2)}\|_F^2 \geq 0$.
- *Positive definiteness:* $\text{dist}_{\tilde{\kappa}}(P^{(1)}, P^{(2)}) = 0$ if and only if $P^{(1)} = P^{(2)}$ in the subspace sense, which means $X^{(1)} = X^{(2)}$.
- *Symmetry:* $\text{dist}_{\tilde{\kappa}}(P^{(1)}, P^{(2)}) = \text{dist}_{\tilde{\kappa}}(P^{(2)}, P^{(1)})$.
- *Triangle inequality:* $\text{dist}_{\tilde{\kappa}}(P^{(1)}, P^{(2)}) + \text{dist}_{\tilde{\kappa}}(P^{(2)}, P^{(3)}) \geq \text{dist}_{\tilde{\kappa}}(P^{(1)}, P^{(3)})$.

Proof. We can prove the properties one by one.

- Assume $\{\phi_1^{(i)}, \phi_2^{(i)}, \dots, \phi_{n^c}^{(i)}\}$ is another orthonormal basis of subspace $X^{(i)}$ with respect to $(\cdot, \cdot)_{\tilde{\kappa}}$ for $i \in 1, 2$. Similarly, we define the orthogonal matrix $\hat{T}^{(i)}$. There is an orthogonal matrix M_i , such that $\hat{T}^{(i)} = T^{(i)} M^{(i)}$. Due to the orthogonal invariant of Frobenius norm, we can see that

$$\begin{aligned} \|(T^{(1)})^\top \tilde{\kappa} \hat{T}^{(2)}\|_F^2 &= \|(T^{(1)})^\top \tilde{\kappa} T^{(2)} M^{(2)}\|_F^2 = \|(T^{(1)})^\top \tilde{\kappa} T^{(2)}\|_F^2 \\ &= \|(M^{(1)})^\top (T^{(1)})^\top \tilde{\kappa} T^{(2)}\|_F^2 = \|(\hat{T}^{(1)})^\top \tilde{\kappa} T^{(2)}\|_F^2, \end{aligned}$$

which means that $\text{dist}_{\tilde{\kappa}}(P^{(1)}, P^{(2)})$ does not depend on the choice of basis.

- Take $B_{kl} = (\psi_k^{(1)}, \psi_l^{(2)})_{\tilde{\kappa}}$, we have

$$\sum_{k=1}^{n^c} B_{kl}^2 \leq \|\psi_l^{(2)}\|_{\tilde{\kappa}}^2 = 1, \quad \sum_{k=1}^{n^c} \sum_{l=1}^{n^c} B_{kl}^2 \leq n^c.$$

Hence, it holds that

$$n^c - \|(T^{(1)})^\top \tilde{\kappa} T^{(2)}\|_F^2 = n^c - \|B\|_F^2 \geq 0.$$

- If $P^{(1)} = P^{(2)}$ in the subspace sense, we have

$$\psi_l^{(2)} = \sum_{k=1}^{n^c} (\psi_k^{(1)}, \psi_l^{(2)})_{\tilde{\kappa}} \psi_k^{(1)}, \quad \sum_{k=1}^{n^c} B_{kl}^2 = \|\psi_l^{(2)}\|_{\tilde{\kappa}}^2 = 1, \quad \sum_{k=1}^{n^c} \sum_{l=1}^{n^c} B_{kl}^2 = n^c,$$

which leads

$$\text{dist}_{\tilde{\kappa}}(P^{(1)}, P^{(2)}) = \sqrt{n^c - \|(T^{(1)})^\top \tilde{\kappa} T^{(2)}\|_F^2} = \sqrt{n^c - \|B\|_F^2} = 0.$$

If

$$\text{dist}_{\tilde{\kappa}}(P^{(1)}, P^{(2)}) = \sqrt{n^c - \|(T^{(1)})^\top \tilde{\kappa} T^{(2)}\|_F^2} = \sqrt{\sum_{l=1}^{n^c} \left(1 - \sum_{k=1}^{n^c} B_{kl}^2\right)} = 0.$$

Due to for all $l \in \{1, 2, 3, \dots, n^c\}$, $1 - \sum_{k=1}^{n^c} B_{kl}^2 \geq 0$, we hence have $1 - \sum_{k=1}^{n^c} B_{kl}^2 = 0$, which means that for all $l \in \{1, 2, 3, \dots, n^c\}$, $\phi_l^{(2)} \in X^{(1)}$. Similarly, we can obtain for all $k = 1, 2, 3, \dots, n^c$, $\phi_k^{(1)} \in X^{(2)}$. Consequently, $P^{(1)} = P^{(2)}$ in the subspace sense.

- Note that $\tilde{\kappa}$ is a diagonal matrix, and we can derive

$$\begin{aligned} \text{dist}_{\tilde{\kappa}}(P^{(1)}, P^{(2)}) &= \sqrt{n^c - \|(T^{(1)})^\top \tilde{\kappa} T^{(2)}\|_F^2} \\ &= \sqrt{n^c - \|(T^{(2)})^\top \tilde{\kappa} T^{(1)}\|_F^2} = \text{dist}_{\tilde{\kappa}}(P^{(2)}, P^{(1)}). \end{aligned}$$

- Denote $\xi_k^{(i)} = \sqrt{\tilde{\kappa}} \psi_k^{(i)}$ and $\{\psi_1^{(i)}, \psi_2^{(i)}, \dots, \psi_{n^c}^{(i)}\}$ is an orthonormal basis of subspace $X^{(i)}$ with respectively to $(\cdot, \cdot)_{\tilde{\kappa}}$, thus $\{\xi_1^{(i)}, \xi_2^{(i)}, \dots, \xi_{n^c}^{(i)}\}$ is an orthonormal basis of subspace $X^{(i)}$ with respectively to l^2 standard inner product. Take matrix $M^{(i)} = \sum_{k=1}^{n^c} \xi_k^{(i)} (\xi_k^{(i)})^\top$, and we can obtain

$$\begin{aligned} \|M^{(i)}\|_F^2 &= n^c, \quad \text{tr}(M^{(p)\top} M^{(q)}) = \sum_{k=1}^{n^c} \sum_{l=1}^{n^c} ((\xi_k^{(p)})^\top \xi_l^{(q)})^2, \\ \|M^{(p)} - M^{(q)}\|_F^2 &= \|M^{(p)}\|_F^2 + \|M^{(q)}\|_F^2 - 2 \text{tr}((M^{(p)})^\top M^{(q)}) \\ &= 2 \text{dist}_{\tilde{\kappa}}^2(P^{(p)}, P^{(q)}). \end{aligned}$$

By triangle inequality for Frobenius norm, it holds that

$$\|M^{(1)} - M^{(3)}\|_F \leq \|M^{(1)} - M^{(2)}\|_F + \|M^{(2)} - M^{(3)}\|_F.$$

Therefore, we can prove the triangle inequality for the distance in the loss function, i.e.,

$$\text{dist}_{\tilde{\kappa}}(P^{(1)}, P^{(2)}) + \text{dist}_{\tilde{\kappa}}(P^{(2)}, P^{(3)}) \geq \text{dist}_{\tilde{\kappa}}(P^{(1)}, P^{(3)}).$$

□

Before we proceed to demonstrate the suitability of our proposed loss function for two-grid preconditioner, it is essential to present some theoretical foundation. To define the performance of the two-grid method, we provide the error operator as follows.

Definition 2. The error operator for two-grid method is given by

$$E = I - B^{-1}A = (I - RA)(I - PA_c^{-1}P^\top A)(I - AR),$$

where B^{-1} is the two-grid preconditioner.

Next, we need to analyze the convergence rate of this error operator, which quantifies the efficiency of the two-grid method. The proof can be found in [32].

Lemma 3.2. *The convergence rate of an exact two-grid method is given by*

$$\|E\|_A^2 = 1 - \frac{1}{K(P)},$$

where

$$K(P) = \max_{v \in \mathbb{R}^N} \min_{v_c \in \mathbb{R}^{N^c}} \frac{\|v - Pv_c\|_{R^{-1}}^2}{\|v\|_A^2}.$$

Building upon the theoretical foundation outlined above, we now establish correlation between the proposed loss function and the convergence rate, which aims to validate the efficacy of the loss function we have introduced.

Theorem 3.3. *Let $E^{(1)}$ and $E^{(2)}$ be the error operators on the prolongation operators $P^{(1)}$ and $P^{(2)}$, respectively. Assume that $P^{(i)} = \text{diag}\{P_1^{(i)}, P_2^{(i)}, \dots, P_n^{(i)}\}$ where $P_j^{(i)}$ is the block of $P^{(i)}$, $P^{(i)} \in \mathbb{R}^{N \times N^c}$ with $\ker(A) \subset \text{im}(P^{(i)})$. Moreover, suppose there exist positive constants C_a , C_1 and C_u , such that $\|\cdot\|_{R^{-1}}^2 \leq C_a \|\cdot\|_A^2$ and $C_1 \|\cdot\|_{\tilde{\kappa}}^2 \leq \|\cdot\|_{R^{-1}}^2 \leq C_u \|\cdot\|_{\tilde{\kappa}}^2$. It holds that*

$$\left| \|E^{(1)}\|_A^2 - \|E^{(2)}\|_A^2 \right| \leq C(C_a, C_u/C_1) \max_j \left\{ \text{dist}_{\tilde{\kappa}_j}^2(P_j^{(1)}, P_j^{(2)}) \right\}.$$

Proof. By Theorem 3.2, we can see that

$$\left| \|E^{(1)}\|_A^2 - \|E^{(2)}\|_A^2 \right| = \left| \frac{K(P^{(2)}) - K(P^{(1)})}{K(P^{(1)})K(P^{(2)})} \right| \leq |K(P^{(2)}) - K(P^{(1)})|,$$

where we utilize the fact that $K(P^{(1)}) \geq 1$ and $K(P^{(2)}) \geq 1$. We are left to bound $|K(P^{(2)}) - K(P^{(1)})|$. To improve the readability of proof, we will omit the index j whenever it does not lead to ambiguity.

Step1 We first introduce the column space $X^{(i)}$ of the prolongation operator $P^{(i)}$ as follows,

$$P^{(i)} = [p_1^{(i)}, p_2^{(i)}, \dots, p_{N^c}^{(i)}], \quad X^{(i)} = \text{span}\{p_1^{(i)}, p_2^{(i)}, \dots, p_{N^c}^{(i)}\}.$$

Under the assumption $N^c < N$ and $\ker(A) \subset \text{im}(P^{(i)})$, it holds that

$$K(P^{(i)}) = \max_{\|v\|_A=1} \min_{v_c \in X^{(i)}} \|v - v_c\|_{R^{-1}}^2.$$

Assume that $\{\phi_1^{(i)}, \phi_2^{(i)}, \dots, \phi_{N^c}^{(i)}\}$ is the orthonormal basis of subspace $X^{(i)}$ but with respect to the inner product $(\cdot, \cdot)_{R^{-1}}$. Then for all $v \in \mathbb{R}^N$ with $\|v\|_A = 1$,

$$v_c^* := \arg \min_{v_c \in X^{(i)}} \|v - v_c\|_{R^{-1}}^2 = \sum_{p=1}^{N^c} (v, \phi_p^{(i)})_{R^{-1}} \phi_p^{(i)},$$

we can obtain $\|v - v_c^*\|_{R^{-1}}^2 = \|v\|_{R^{-1}}^2 - \sum_{p=1}^{N^c} (v, \phi_p^{(i)})_{R^{-1}}^2$. Under the assumption $\|\cdot\|_{R^{-1}}^2 \leq C_a \|\cdot\|_A^2$, it yields $\|v_c^*\|_{R^{-1}}^2 \leq \|v\|_{R^{-1}}^2 \leq C_a \|v\|_A^2 \leq C_a$.

Step2 By scaling $K(P^{(1)})$, we can obtain

$$\begin{aligned} K(P^{(1)}) &= \max_{\|v\|_A=1} \min_{v_{c_1} \in X^{(1)}} \|v - v_{c_1}\|_{R^{-1}}^2 \\ &\leq \max_{\|v\|_A=1} \min_{v_{c_1} \in X^{(1)}} \left(\|v - v_{c_2}\|_{R^{-1}}^2 + \|v_{c_2} - v_{c_1}\|_{R^{-1}}^2 \right) \\ &\leq \max_{\|v\|_A=1} \left(\|v - v_{c_2}\|_{R^{-1}}^2 + \min_{v_{c_1} \in X^{(1)}} \|v_{c_2} - v_{c_1}\|_{R^{-1}}^2 \right) \\ &\leq \underbrace{\max_{\|v\|_A=1} \|v - v_{c_2}\|_{R^{-1}}^2}_{K_1} + \underbrace{\max_{\|v\|_A=1} \min_{v_{c_1} \in X^{(1)}} \|v_{c_2} - v_{c_1}\|_{R^{-1}}^2}_{K_2}. \end{aligned}$$

Let $v_{c_2} = \arg \min_{v_{c_2} \in X^{(2)}} \|v - v_{c_2}\|_{R^{-1}}^2 = \sum_{p=1}^{N^c} (v, \phi_p^2)_{R^{-1}} \phi_p^2$, and take it into K_1 and K_2 . For K_1 ,

$$\max_{\|v\|_A=1} \|v - \sum_{p=1}^{N^c} (v, \phi_p^2)_{R^{-1}} \phi_p^2\|_{R^{-1}}^2 = \max_{\|v\|_A=1} \min_{v_{c_2} \in X^{(2)}} \|v - v_{c_2}\|_{R^{-1}}^2 = K(P^{(2)}).$$

For K_2 , recalling that $\|v_{c_2}\|_{R^{-1}}^2 \leq C_a$, we have

$$\begin{aligned} & \max_{\|v\|_A=1} \min_{v_{c_1} \in X^{(1)}} \left\| \sum_{p=1}^{N^c} (v, \phi_p^2)_{R^{-1}} \phi_p^2 - v_{c_1} \right\|_{R^{-1}}^2 \\ & \leq \max_{v \in X^{(2)}, \|v\|_{R^{-1}} \leq \sqrt{C_a}} \min_{v_{c_1} \in X^{(1)}} \|v - v_{c_1}\|_{R^{-1}}^2 \\ & = C_a \max_{v \in X^{(2)}, \|v\|_{R^{-1}} \leq 1} \min_{v_{c_1} \in X^{(1)}} \|v - v_{c_1}\|_{R^{-1}}^2. \end{aligned}$$

By the assumption $C_1 \|\cdot\|_{\tilde{\kappa}}^2 \leq \|\cdot\|_{R^{-1}}^2 \leq C_u \|\cdot\|_{\tilde{\kappa}}^2$,

$$\begin{aligned} K(P^{(1)}) & \leq K(P^{(2)}) + C_a \max_{v \in X^{(2)}, \|v\|_{R^{-1}} \leq 1} \min_{v_{c_1} \in X^{(1)}} \|v - v_{c_1}\|_{R^{-1}}^2 \\ & \leq K(P^{(2)}) + \frac{C_a C_u}{C_1} \max_{v \in X^{(2)}, \|v\|_{\tilde{\kappa}} \leq 1} \min_{v_{c_1} \in X^{(1)}} \|v - v_{c_1}\|_{\tilde{\kappa}}^2. \end{aligned}$$

Due to the symmetry of $P^{(1)}$, $P^{(2)}$, we can also derive

$$K(P^{(2)}) \leq K(P^{(1)}) + \max_{v \in X^{(1)}, \|v\|_{\tilde{\kappa}} \leq 1} \min_{v_{c_2} \in X^{(2)}} \frac{C_a C_u}{C_1} \|v - v_{c_2}\|_{\tilde{\kappa}}^2.$$

Step3 Take $\{\psi_1^{(i)}, \psi_2^{(i)}, \dots, \psi_{N^c}^{(i)}\}$ as an orthonormal basis of subspace $X^{(i)}$ with respect to $(\cdot, \cdot)_{\tilde{\kappa}}$. For all $v \in X^{(2)}$, introducing the expansion $v = \sum_{p=1}^{N^c} a_p \psi_p^{(2)}$ with $\|v\|_{\tilde{\kappa}}^2 = \sum_{p=1}^{N^c} a_p^2$, we can show that

$$\max_{v \in X^{(2)}, \|v\|_{\tilde{\kappa}} \leq 1} \min_{v_{c_1} \in X^{(1)}} \|v - v_{c_1}\|_{\tilde{\kappa}}^2 = \max_{\sum_p a_p^2=1} \sum_{p=1}^{N^c} a_p^2 \left(1 - \sum_{q=1}^{N^c} (\psi_p^{(2)}, \psi_q^{(1)})_{\tilde{\kappa}}^2 \right).$$

Utilizing the non-overlapping properties of coarse elements, we can divide a_p , $\psi_p^{(2)}$ and $\psi_q^{(1)}$ into $a_{j,k}$, $\psi_{j,k}^{(2)}$ and $\psi_{j,l}^{(1)}$ respectively, where $j = 1, 2, \dots, n$ and $k = 1, 2, \dots, n^c$, $l = 1, 2, \dots, n^c$. Then, we can derive

$$\begin{aligned} & \max_{\sum_p a_p^2=1} \sum_{p=1}^{N^c} a_p^2 \left(1 - \sum_{q=1}^{N^c} (\psi_p^{(2)}, \psi_q^{(1)})_{\tilde{\kappa}}^2 \right) \\ & = \max_{\sum_{j,k} a_{j,k}^2=1} \sum_{j=1}^n \sum_{k=1}^{n^c} a_{j,k}^2 \left(1 - \sum_{l=1}^{n^c} (\psi_{j,k}^{(2)}, \psi_{j,l}^{(1)})_{\tilde{\kappa}_j}^2 \right) \\ & \leq \max_j \left\{ \max_{\sum_k a_{j,k}^2=1} \sum_{k=1}^{n^c} a_{j,k}^2 \left(1 - \sum_{l=1}^{n^c} (\psi_{j,k}^{(2)}, \psi_{j,l}^{(1)})_{\tilde{\kappa}_j}^2 \right) \right\} \leq \max_j \left\{ \text{dist}_{\tilde{\kappa}_j}^2 (P_j^{(1)}, P_j^{(2)}) \right\}. \end{aligned}$$

Follow a similar procedure, we can also obtain

$$\max_{v \in X_1, \|v\|_{\tilde{\kappa}} \leq 1} \min_{v_{c_2} \in X_2} \|v - v_{c_2}\|_{\tilde{\kappa}}^2 \leq \max_j \left\{ \text{dist}_{\tilde{\kappa}_j}^2 (P_j^{(1)}, P_j^{(2)}) \right\}.$$

Combining all results above, we hence complete the proof. \square

3.3 Data augmentation

In deep learning, the challenge of limited training data is pervasive. To address this, we can artificially expand the training dataset through a series of transformations known as data augmentation. Depending on the specific problem at hand, we recommend employing symmetry transformation and Karhunen–Loève expansion as methods for implementing data augmentation. These techniques not only diversify the dataset but also enhance the model’s ability to generalize from limited data inputs.

3.3.1 Symmetry transformation

In the context of the LSP, we observe inherent symmetries when the computational domain is partitioned appropriately. In this study, we set $h_x = h_y$ to ensure that symmetric variations such as row symmetry, column symmetry, principal diagonal symmetry, and auxiliary diagonal symmetry are effectively considered.

Theorem 3.4. *By taking $\tilde{\kappa} = \kappa$ in Eq. (5), the LSP satisfies the following symmetric invariant relation: Let \mathcal{T} be one of the symmetric variations which contains row symmetry, column symmetry, principal diagonal symmetry and auxiliary diagonal symmetry; If the pair (λ^k, Φ_k) is the solution of Eq. (5) based on κ , $(\lambda^k, \mathcal{T}\Phi_k)$ is the solution of Eq. (5) based on $\mathcal{T}\kappa$.*

Proof. The symmetric variations are one-to-one such that for the right-hand side,

$$\lambda^k \int_{K_j} \kappa \Phi_k w_h \, d\mathbf{x} = \lambda^k \int_{K_j} (\mathcal{T}\kappa)(\mathcal{T}\Phi_k)(\mathcal{T}w_h) \, d\mathbf{x}, \quad \forall w_h \in W_h(K_j). \quad (6)$$

For the left-hand side, in Fig. 4, we can observe that the symmetric variations \mathcal{T} do not alter the neighbor pairs of the edge set. This implies that if $(\kappa_{e,-}, \kappa_{e,+})$ is a neighbor pair of an edge $e \in \mathcal{E}^h(K_j)$, then $(\mathcal{T}\kappa_{e,-}, \mathcal{T}\kappa_{e,+})$ remains a neighbor pair of an edge $e \in \mathcal{E}^h(\mathcal{T}K_j)$. Therefore, we can see that

$$\sum_{e \in \mathcal{E}^h(K_j)} \kappa_e \llbracket \Phi_k \rrbracket_e \llbracket w_h \rrbracket_e = \sum_{e \in \mathcal{E}^h(\mathcal{T}K_j)} (\mathcal{T}\kappa)_e \llbracket \mathcal{T}\Phi_k \rrbracket_e \llbracket \mathcal{T}w_h \rrbracket_e, \quad \forall w_h \in W_h(K_j). \quad (7)$$

Combine Eq. (6) and Eq. (7),

$$\sum_{e \in \mathcal{E}^h(K_j)} (\mathcal{T}\kappa)_e \llbracket \mathcal{T}\Phi_k \rrbracket_e \llbracket \mathcal{T}w_h \rrbracket_e = \lambda^k \int_{K_j} (\mathcal{T}\kappa)(\mathcal{T}\Phi_k)(\mathcal{T}w_h) \, d\mathbf{x}, \quad \forall w_h \in W_h(K_j), \quad (8)$$

which also can be written as

$$\sum_{e \in \mathcal{E}^h(K_j)} (\mathcal{T}\kappa)_e \llbracket \mathcal{T}\Phi_k \rrbracket_e \llbracket w_h \rrbracket_e = \lambda^k \int_{K_j} (\mathcal{T}\kappa)(\mathcal{T}\Phi_k)w_h \, d\mathbf{x}, \quad \forall w_h \in W_h(\mathcal{T}K_j). \quad (9)$$

□

Remark. If $h_x \neq h_y$, Theorem 3.4 still holds for row symmetry and column symmetry. It requires that \mathcal{T} variation remains unchanged in the horizontal and vertical directions of the edges.

Drawing on the insights gained, we have augmented the dataset by implementing transformations such as row symmetry, column symmetry, principal diagonal symmetry, and auxiliary diagonal symmetry to the data within the training set. Furthermore, the augmented data does not require separate label generation, significantly reducing the time required for training neural networks.

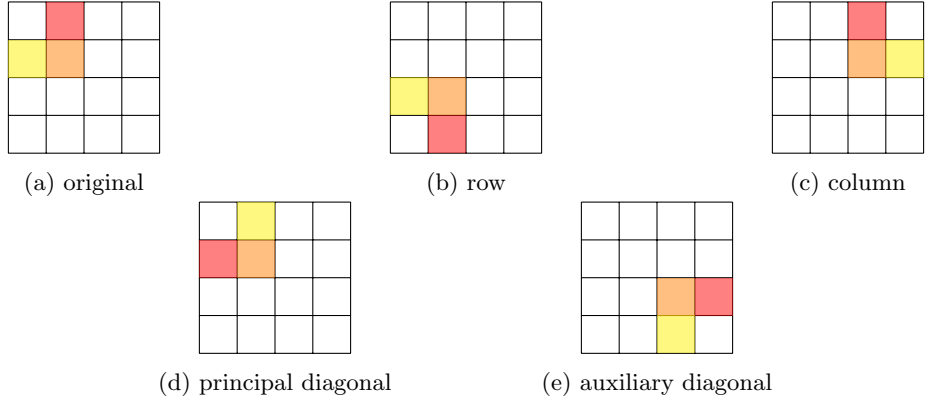


Figure 4: Examples of symmetry transformation of 4×4 grid.

3.3.2 Karhunen–Loève expansion

The augmentation effect of symmetry transformation on data is limited. For example, the mentioned symmetry methods can at most quadruple the original dataset. When the data volume is still insufficient, one effective approach is to use the Karhunen–Loève expansion to numerically approximate random field $\kappa(\mathbf{x}; \omega)$ by utilizing discrete data reconstruction. Karhunen–Loève expansion seeks to represent a random field through a linear combination of a set of orthogonal basis functions. To ensure positive permeability in the computational domain Ω , we take $Z(\mathbf{x}; \omega) = \log \kappa(\mathbf{x}; \omega)$ and assume that $Z(\mathbf{x}; \omega)$ is a Gaussian field. To construct the Karhunen–Loève expansion of $Z(\mathbf{x}; \omega)$, we need to solve the following spectral problem

$$\int_{\Omega} \mathbb{C}_Z(\mathbf{x}, \mathbf{y}) f(\mathbf{y}) d\mathbf{y} = \mu f(\mathbf{x}),$$

where $\mathbb{C}_Z(\mathbf{x}, \mathbf{y})$ is the covariance kernel function and eigenpairs (μ^α, f_α) are obtained. The number of total eigenpairs is equal to the degree of freedom of fine meshes, i.e., N in our setting. The Karhunen–Loève expansion can be expressed as $Z(\mathbf{x}; \omega) = \mathbb{E}[Z](\mathbf{x}) + \sum_{\alpha=1}^N \omega_\alpha \sqrt{\mu^\alpha} f_\alpha(\mathbf{x})$, where $\mathbb{E}[Z](\mathbf{x})$ is the mean value function, ω_α are random variables with zero mean and unit variance. For data augmentation, we take the l -truncated Karhunen–Loève expansion

$$Z(\mathbf{x}; \omega) \approx \mathbb{E}[Z](\mathbf{x}) + \sum_{\alpha=1}^l \omega_\alpha \sqrt{\mu^\alpha} f_\alpha(\mathbf{x}), \quad (10)$$

where $\{\mu^1, \mu^2, \dots, \mu^l\}$ are the l largest eigenvalues. Consequently, the key of reconstruct random field is estimating the mean function and the covariance kernel function by some samples. Denote $\{Z_1(\mathbf{x}), Z_2(\mathbf{x}), \dots, Z_m(\mathbf{x})\}$ as m samples, and we present the estimations for $\mathbb{E}[Z](\mathbf{x})$ and $\mathbb{C}_Z(\mathbf{x}, \mathbf{y})$ as follows,

$$\begin{aligned} \hat{\mathbb{E}}[Z](\mathbf{x}) &= \frac{1}{m} \sum_{s=1}^m Z_s(\mathbf{x}), \\ \hat{\mathbb{C}}_Z(\mathbf{x}, \mathbf{y}) &= \frac{1}{m} \sum_{s=1}^m \left[\left(Z_s(\mathbf{x}) - \hat{\mathbb{E}}[Z](\mathbf{x}) \right) \left(Z_s(\mathbf{y}) - \hat{\mathbb{E}}[Z](\mathbf{y}) \right) \right] \end{aligned} \quad (11)$$

which will be substituted into the Karhunen–Loève expansion construction.

4 Numerical experiments

All neural network training is conducted on a single Nvidia A100-PCIE-40GB GPU, while the remaining iterative solving processes are performed on a desktop with an Intel Core i9-12900 CPU. This arrangement is

primarily due to the relatively small scale of the cases, which makes it difficult to fully utilize the GPU’s high parallel computing power, meanwhile it also helps to reduce unnecessary energy consumption and improves resource efficiency. The neural network training is implemented using PyTorch, while the iterative solver is based SciPy’s sparse matrix routines.

In our simulations, we consider a heterogeneous computational domain $\Omega = [0, 1] \times [0, 1]$ with uncertainties. Our square coarse grid \mathcal{T}_H is of the size 16×16 and its refinement fine grid \mathcal{T}_h is of 512×512 squares which means that each coarse element contains 32×32 fine elements. Note that the smallest eigenvalue is always 0 and the corresponding eigenvector is a constant function. Therefore, we only need to generate $n^c - 1$ local generalized multiscale basis by neural networks. According to [34], choosing $n^c = 5$ is sufficient to achieve robustness while maintaining efficiency. Hence, we set $n^c = 5$ as the default value in our experiments. The training ends after 30 epochs.

4.1 Prolongation operator learning experiments

4.1.1 Log-Gaussian random field

Consider the logarithm of the random coefficients following a Gaussian random field, which has a mean function of zero and covariance kernel function is

$$\mathbb{C}_Z(\mathbf{x}, \mathbf{y}) = \sigma^2 \exp\left(-\sqrt{\frac{|x_1 - y_1|^2}{\eta_1^2} + \frac{|x_2 - y_2|^2}{\eta_2^2}}\right),$$

where $Z(\mathbf{x}; \omega) = \log \kappa(\mathbf{x}; \omega)$, $\mathbf{x} = (x_1, x_2)$, $\mathbf{y} = (y_1, y_2)$, $\sigma^2 = 2$, η_1 and η_2 correlation lengths in each direction of space.

We sample a total of 200 instances of $\kappa(\mathbf{x}; \omega)$ from the Log-Gaussian random field to construct our dataset. This includes 180 samples designated for the training dataset, with each κ further subdivided into 16^2 coarse elements, yielding a total of 46080 examples. The remaining 20 samples are allocated to the test dataset, resulting in 5120 examples. As illustrated in Fig. 5, deeper neural networks generally yield superior results. Notably, the performance of the two-level U-Net is significantly distinct from that of the three-level and four-level U-Net. Although the improvements between the three-level and four-level U-Net are relatively modest, the four-level U-Net is preferred due to its superior performance.

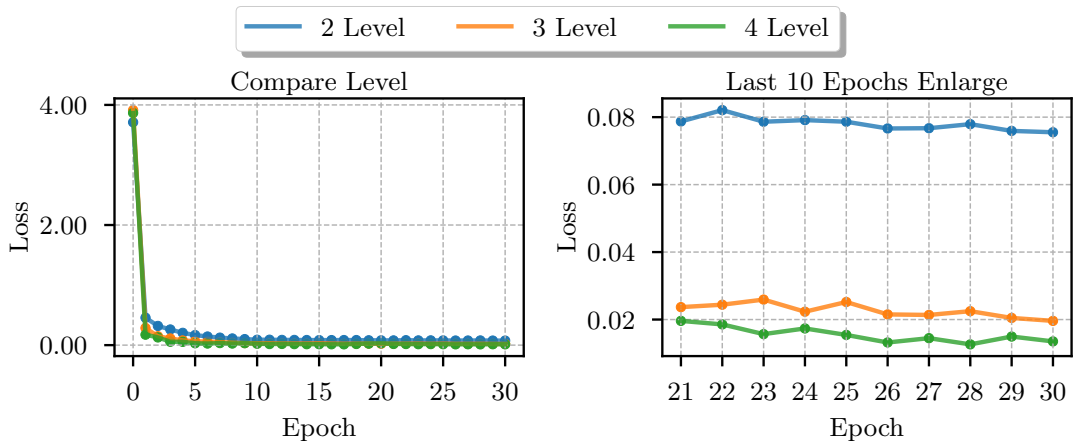


Figure 5: Test loss for neural networks of varying depths on the same dataset is displayed in two parts: **left part** shows results across all 30 epochs, and **right part** presents an enlarged view of the results for the last 10 epochs.

The number of training parameters and the training time required for different levels of U-Net architectures are summarized in Table 1. As anticipated, both the number of training parameters and the training time increase with the depth of the neural network. However, the training time does not scale directly proportionally to the number of training parameters, which we attribute to the parallel computing capabilities and the design of the U-Net architecture. Additionally, we highlight that by leveraging GPUs, all training are finished within 2 minutes.

Table 1: The number of training parameters and the total training time of different levels of U-Net architectures.

U-Net depth	Training parameters (M)	Training time (s)
2-Level	0.11	83.10
3-Level	0.52	97.49
4-Level	2.14	106.75

In situations where training data are scarce, we employ symmetry transformation as a data augmentation technique. Specifically, we initially sample only 36 instances of $\kappa(\mathbf{x}; \omega)$ from Log-Gaussian random field to form our training dataset, while the test dataset remains unchanged. We then substantially expand this dataset through symmetry transformation. As indicated in Fig. 6, after applying symmetry transformation for data augmentation, there is a noticeable improvement in the performance of the two-level, three-level, and four-level U-Net architectures on the test set. This enhancement substantiates the efficacy of symmetry transformation as a method for data augmentation.

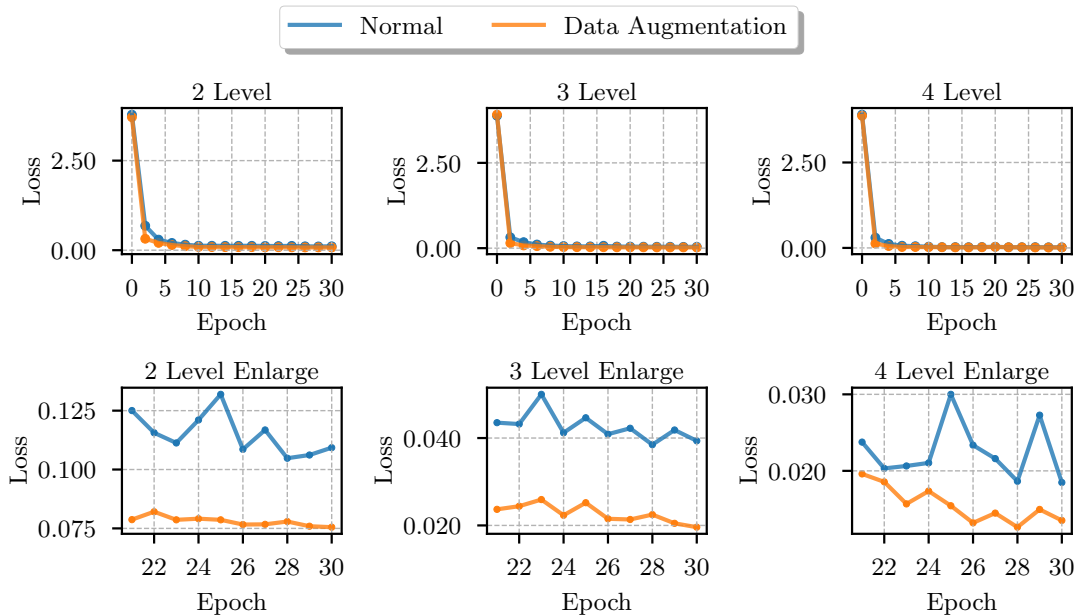


Figure 6: Evaluate the impact of data augmentation on test loss for neural networks of varying depths by examining the differences before and after augmentation on the same test dataset. **Above part** displays the test loss trajectories for neural networks of different depths throughout all 30 training epochs. **Below part** offers an expanded view of the test loss for the final 10 epochs.

As previously noted, due to inherent symmetries in the solutions of the LSP, we can avoid label generation for the augmented training data, significantly reducing the time required for generating neural networks models. In our experiment setup, we compare two methods to generate the *same amount* of training data

for neural networks training: one involves sampling exclusively from Log-Gaussian random field and another one combines direct sampling from Log-Gaussian random field for 1/5 of the data with the remaining 4/5 generated through symmetry transformation augmentation. The loss is calculated on the same test dataset. According to the results shown in Fig. 7, using symmetry transformation to generate labels for the training set does not negatively impact the accuracy. Furthermore, the training set augmented with symmetry transformations exhibits more stable performance during testing.

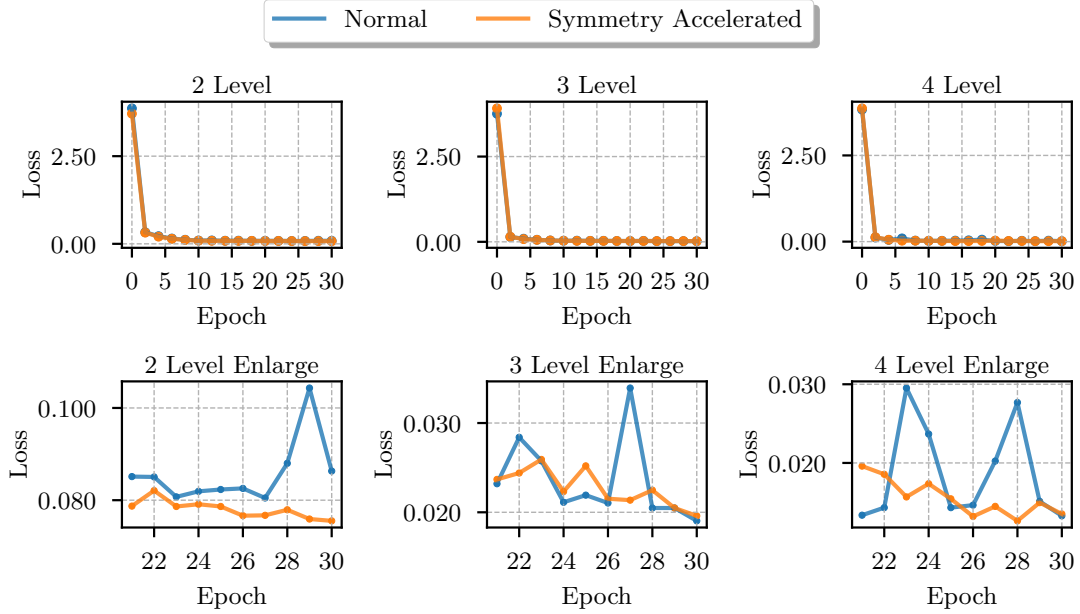


Figure 7: Compare the test loss between training data all from random field and some data from augmentation for neural networks of different depths on the same test dataset. **Above part** displays the test loss trajectories for neural networks of different depths throughout all 30 training epochs. **Below part** offers an expanded view of the test loss for the final 10 epochs.

Next, we opt for the four-level U-Net architecture, sampling 56 instances of $\kappa(\mathbf{x};\omega)$, with 36 samples designated for the training set, which is augmented using symmetry transformations, and 20 samples are allocated to the test set. A sample of the results from the four-level U-Net, depicted in Fig. 8, reveals outcomes that closely resemble the generalized multiscale subspace derived from the LSP, illustrating the effectiveness of this architecture in capturing the essential characteristics of the data.

4.1.2 Random disk inclusion coefficients

In the subsequent experiments, we consider the presence of 15 non-overlapping disks in the computational domain Ω . The locations and radii of these disks are randomly assigned. The permeability value in disks, denoted κ_b , contrasts significantly with the rest of the domain where κ is set to 1, referred to as κ_r . The coefficient κ of the resolution 512×512 fine grid is determined by the following rules:

- Elements entirely within or outside the disks adopt κ_b and κ_r respectively.
- For elements intersecting the boundaries of these disks, the effective permeability, $\kappa_{\text{element}}^{-1}$, is calculated as the harmonic mean of κ_b^{-1} and κ_r^{-1} .

We test κ_b chosen from $\{10^5, 10^4, 10^3, 10^2, 10^{-2}, 10^{-3}, 10^{-4}, 10^{-5}\}$. This setting introduces a significantly higher contrast in κ values compared to those derived from Log-Gaussian random field, aiming to assess the model's capability to handle extreme contrast in permeability.

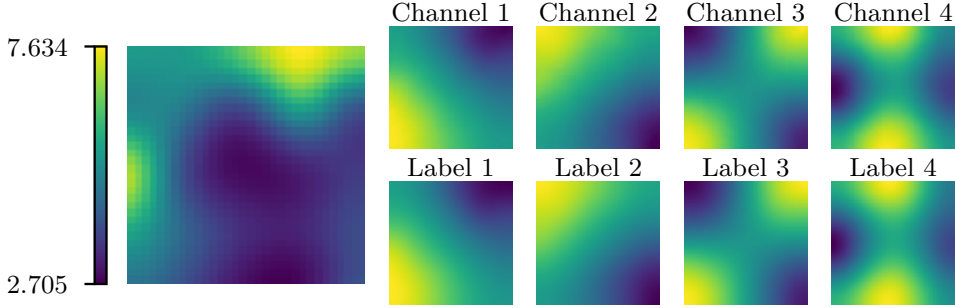


Figure 8: A sample of an input coarse element from the test set is shown on the left. The labels are derived from the LSP, and the channels represent the projection of the corresponding labels onto the generalized multiscale subspace learned by the four-level U-Net.

We sample 56 instances of $\kappa(\mathbf{x};\omega)$ by randomly creating disks within the computational domain. Of these, 36 samples are designated for the training set and augmented through symmetry transformation, while the remaining 20 samples are reserved for the test set. The performance of the four-level U-Net across varying κ_b values is depicted in Fig. 9. As expected, lower contrast cases yield better performance, but only minor differences are observed compared to higher contrast cases.

We here consider apply Karhunen–Loève expansion for data augmentation on this random coefficient setting. Let K represent the K -truncated Karhunen–Loève expansion as in Eq. (10), and let M denote the multiplication factor required to augment the training dataset. Specifically, we take $46080/M$ coarse elements from a training set generated by random disks, reconstruct the random field as Eq. (11) the $46080/M$ coarse elements and augment the training data to 46080. From Fig. 10, we observe that increasing the truncation level K of Karhunen–Loève expansion enhances its effectiveness in augmenting the dataset. Specifically, when K reaches 25, the performance of the model closely approximates that of the training conducted without employing the Karhunen–Loève expansion. This finding suggests that a K -value of 25 provides a sufficient approximation of the underlying random field, enabling substantial improvements in model training by capturing essential features within the data. We also investigate the effect of varying the data augmentation factor M on the model’s performance. In Fig. 11, the results for the four-level U-Net, which is trained using a dataset expanded by a factor of 2 to 100 through the application of a 25-truncated Karhunen–Loève expansion are reported. Performance remains sufficiently effective at different values of M , although deterioration is observed when M is large. This approach highlights the robustness of the Karhunen–Loève expansion in enhancing the training process under conditions of substantial data augmentation.

We also virtualize the output of neural networks in this random coefficient setting. The dataset comprises 56 instances of $\kappa(\mathbf{x};\omega)$, with 36 samples designated for the training set, which is enhanced using symmetry transformations, and 20 samples are allocated to the test set. It presents samples of κ_b values from 10^{-5} to 10^{-2} in Fig. 12. These samples exhibit characteristics that are notably similar to the generalized multi-scale subspace derived from the LSP. Similarly, for κ_b values between 10^2 and 10^5 , the results are equally promising, and due to space constraints, are not presented here.

4.2 Preconditioner comparison

In this section, we examine the efficacy of a prolongation operator generated by the four-level U-Net in two-grid preconditioner and compare its performance to other preconditioners. All types of preconditioners are integrated within the PCG iteration scheme, which is employed to solve equations with the no-flux boundary condition. The source term f is assigned values of 1 in the top-left and bottom-right fine elements, -1 in the bottom-left and top-right fine elements, and 0 elsewhere. The PCG with a two-grid preconditioner is

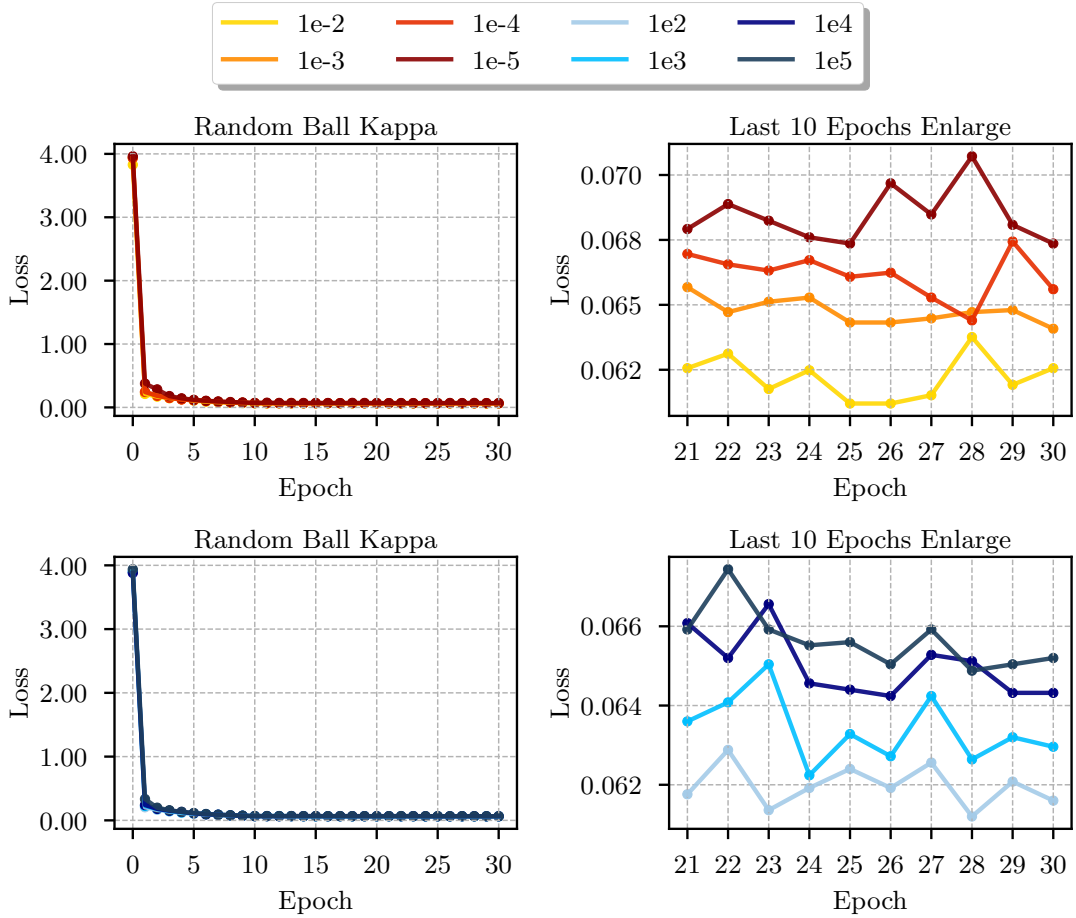


Figure 9: Test loss for different κ_b values using the four-level U-Net is displayed in two parts: **left part** shows results across all 30 epochs, and **right part** presents an enlarged view of the results for the last 10 epochs.

accompanied by a Block-Jacobi smoother, with the block size tailored to the coarse elements' dimensions. The relative tolerance is set to 10^{-6} . The coefficient profiles are generated following the same procedure as in the previous section, and we adopt notations “Gaussian RF” and “RB” to represent the Log-Gaussian random field and random disk inclusion coefficient respectively. Each experiment is repeated 10 times, and the time records presented below are the averages of these repeated experiments.

We first test the two-grid preconditioner with the prolongation operator generated by the four-level U-Net. Additionally, we compare the iteration counts (iteration time) with the prolongation operators generated by precisely solving LSPs with 1, 3 and 5 bases. As depicted in Table 2, in terms of iteration counts, the prolongation operator produced by the four-level U-Net exhibits performance on par with that derived from 5 basis functions in each LSP, and it significantly outperforms the operators derived from either one or three basis functions in each LSP. Importantly, we observe actual acceleration on solution time up to 50% by using neural network techniques.

We then compare the iteration counts (iteration time) with two easily obtainable preconditioners on the Python platform, which are pyAMG, a Python implementation of algebraic multigrid methods [6], and ILU, an incomplete LU decomposition provided in SciPy. We specially take the ILU(10) preconditioner as a representative of the ILU family. In Table 3, we observe that, as the contrast of κ increases, the

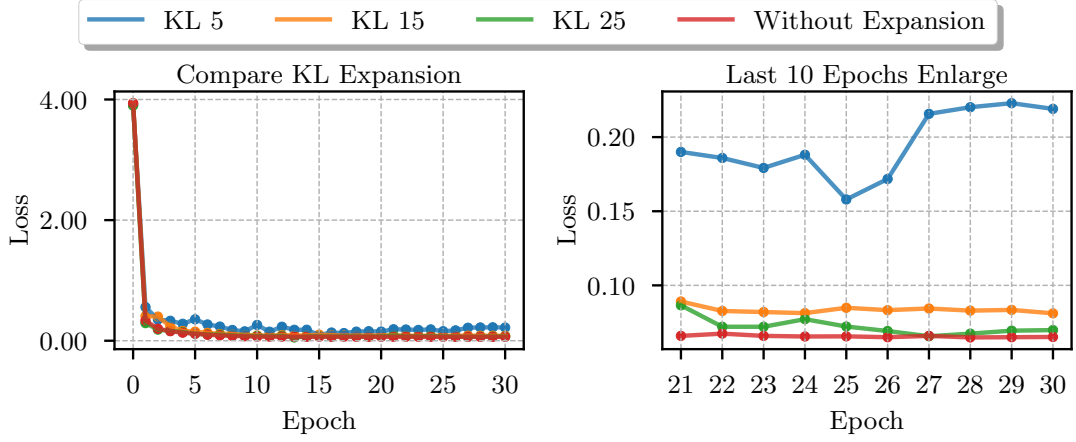


Figure 10: The test loss for the four-level U-Net, trained with $\kappa_b = 10^4$, and data augmentation factor $M = 2$, across different truncation levels K of Karhunen–Loève expansion is displayed in two parts: **left part** shows results across all 30 epochs, and **right part** presents an enlarged view of the results for the last 10 epochs.

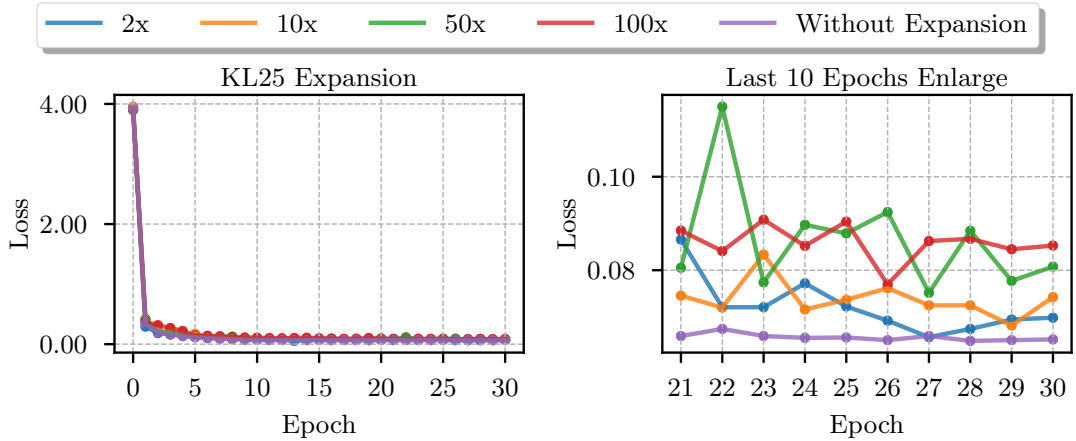


Figure 11: The test loss for a four-level U-Net, trained with $\kappa_b = 10^4$, and truncation level $K = 25$, across varying data augmentation factors M is displayed in two parts: **left part** shows results across all 30 epochs, and **right part** presents an enlarged view of the results for the last 10 epochs.

two-grid preconditioner gradually outperforms the ILU(10) preconditioner and the AMG preconditioner in terms of iteration counts. However, due to the time-consuming process of solving LSPs to generate the prolongation operator, it does not exhibit an advantage in terms of iteration time. Nonetheless, by employing neural networks acceleration to generate the prolongation operator for the two-grid preconditioner, when the contrast of κ reaches 10^4 , the accelerated two-grid preconditioner outperforms both the ILU(10) preconditioner and the pyAMG preconditioner in terms of both iteration counts and iteration time. This result demonstrates the potential of proposed method in solving large linear systems with high-contrast coefficients.

In Table 4, we present a comparative analysis of the average time consumption involved in obtaining the prolongation operator from the test dataset using the four-level U-Net versus the time taken to solve

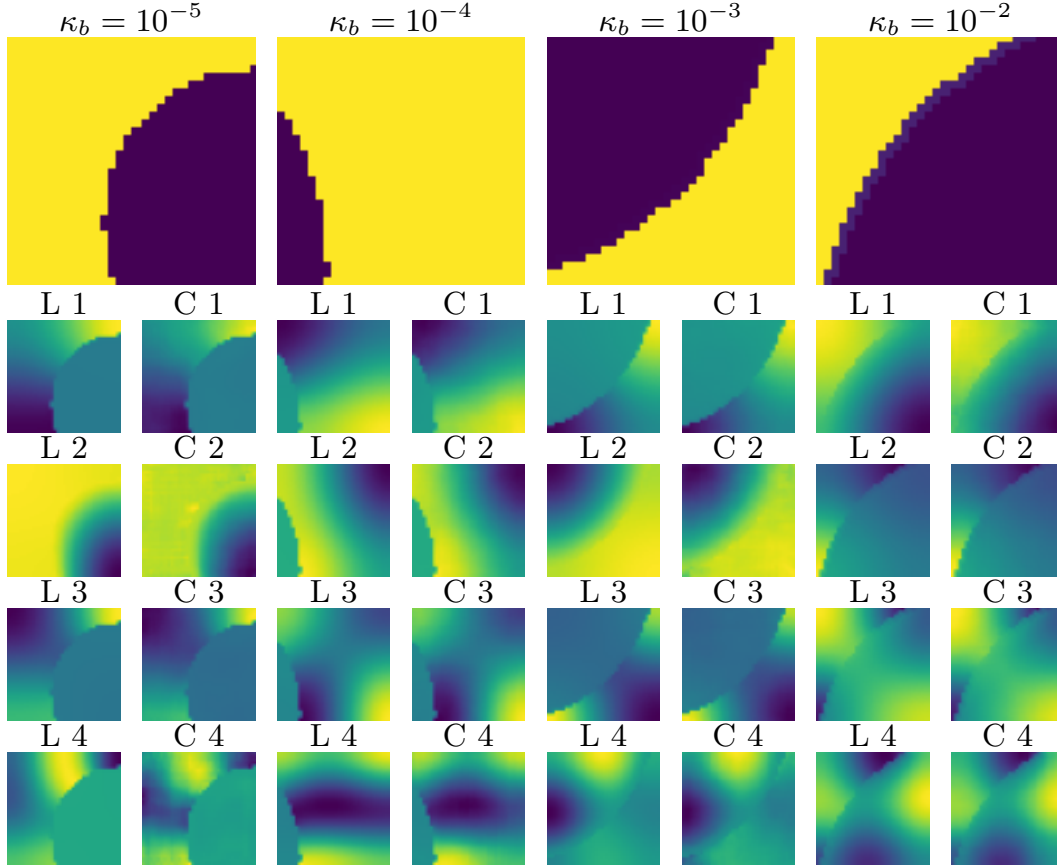


Figure 12: Samples of input coarse elements (κ_b values from 10^{-5} to 10^{-2}) from test set shows in left part, L1 to L4 are derived from the LSP and C1 to C4 represent the projection of the corresponding labels onto the generalized multiscale subspace learned by the four-level U-Net.

Table 2: Iteration counts and computing time for the two-grid preconditioner with the prolongation operators generated by solving LSPs precisely and the four-level U-Net, where “1-LSP-MG”, “3-LSP-MG”, “5-LSP-MG” and “5-NN-MG” represent the prolongation operators derived from LSPs with 1, 3, 5 bases and the four-level U-Net respectively.

Coefficient profiles	1-LSP-MG	3-LSP-MG	5-LSP-MG	5-NN-MG
Gaussian RF	67 (11.92)	22 (7.49)	12 (6.19)	13 (3.06)
RB $\kappa_b = 10^2$	67 (11.62)	29 (8.85)	17 (7.08)	19 (3.89)
RB $\kappa_b = 10^{-2}$	68 (11.70)	24 (7.76)	16 (7.13)	17 (3.68)
RB $\kappa_b = 10^3$	72 (12.88)	29 (9.11)	19 (7.40)	21 (4.33)
RB $\kappa_b = 10^{-3}$	71 (12.11)	24 (8.03)	17 (7.16)	17 (3.78)
RB $\kappa_b = 10^4$	77 (13.41)	30 (8.90)	19 (7.74)	21 (4.39)
RB $\kappa_b = 10^{-4}$	82 (14.43)	27 (8.19)	17 (7.45)	18 (3.92)
RB $\kappa_b = 10^5$	136 (23.40)	34 (9.76)	21 (8.00)	23 (4.77)
RB $\kappa_b = 10^{-5}$	121 (21.06)	29 (9.13)	20 (7.85)	23 (4.82)

LSPs. The results indicate that the four-level U-Net architecture significantly reduces the time required to generate the prolongation operator.

Table 3: Iteration counts and computing time for ILU(10), pyAMG, the two-grid preconditioner by solving LSPs precisely, and two-grid preconditioner by the four-level U-Net.

Coefficient profiles	ILU(10)	pyAMG	5-LSP-MG	5-NN-MG
Gaussian RF	17 (3.26)	6 (2.50)	12 (6.19)	13 (3.06)
RB $\kappa_b = 10^2$	38 (3.89)	15 (2.78)	17 (7.08)	19 (3.89)
RB $\kappa_b = 10^{-2}$	32 (3.77)	14 (2.74)	16 (7.13)	17 (3.68)
RB $\kappa_b = 10^3$	107 (5.21)	48 (3.64)	19 (7.40)	21 (4.33)
RB $\kappa_b = 10^{-3}$	123 (5.57)	44 (3.58)	17 (7.16)	17 (3.78)
RB $\kappa_b = 10^4$	276 (9.74)	62 (4.51)	19 (7.74)	21 (4.39)
RB $\kappa_b = 10^{-4}$	285 (9.26)	59 (4.14)	17 (7.45)	18 (3.92)
RB $\kappa_b = 10^5$	528 (13.64)	101 (6.18)	21 (8.00)	23 (4.77)
RB $\kappa_b = 10^{-5}$	527 (14.80)	82 (5.79)	20 (7.85)	23 (4.82)

Table 4: Comparison of time consumption for solving LSPs and NN across different datasets.

Data Set	Time for Solving LSP (s)	Time for NN (s)
Log-Gaussian Random Fields	4.2791	0.8379
RB $\kappa_b = 1 : 10^{-5}$	4.2885	0.8834
RB $\kappa_b = 1 : 10^{-4}$	4.2973	0.8929
RB $\kappa_b = 1 : 10^{-3}$	4.1959	0.8405
RB $\kappa_b = 1 : 10^{-2}$	4.2318	0.8532
RB $\kappa_b = 1 : 10^2$	4.2302	0.8381
RB $\kappa_b = 1 : 10^3$	4.1966	0.8426
RB $\kappa_b = 1 : 10^4$	4.2201	0.8348
RB $\kappa_b = 1 : 10^5$	4.2492	0.8598
Average	4.2709	0.8537

4.3 Generalization ability tests

We first evaluate the generalization ability on different resolutions of the coarse element. The neural networks we designed is trained by coarse elements of size 32×32 , yet it remains applicable to smaller coarse elements. To adapt these smaller elements to the required input size of the network, one can employ nearest neighbor interpolation. The resulting outputs can then be refined to the target dimensions through mean downsampling. We evaluate coarse elements of sizes of 16×16 and 8×8 , which are extracted from the Gaussian RF coefficients. The reports are presented in Table 5. For smaller coarse elements, the two-grid preconditioner derived from the pre-trained four-level U-Net model requires slightly more iterations to converge than that derived from precisely solved 5 basis functions, while fewer iterations than those derived from 3 or 1 basis function(s) in each LSP. While regarding iteration time, the pre-trained four-level U-Net model exhibits a notable acceleration.

Table 5: Iteration counts and computing time on different coarse element sizes for the two-grid preconditioner with the prolongation operators generated by solving LSPs precisely and the pre-trained four-level U-Net model.

Coarse element sizes	1-LSP-MG	3-LSP-MG	5-LSP-MG	5-NN-MG
16×16	38 (6.92)	13 (6.49)	7 (5.58)	8 (2.88)
8×8	23 (5.96)	9 (6.02)	5 (5.59)	7 (2.61)

We then evaluate the generalization ability of the neural network model on coefficients that fall outside the training set distribution. Specifically, we test the model trained on the Gaussian RF dataset using the RB test set. As shown in ??, although some performance degradation is observed, the results confirm a significant acceleration in computation time. This suggests that the neural network effectively replaces the nonlinear process of solving the LSP and does not heavily rely on κ following a specific distribution. We

believe this finding is highly promising and warrants further in-depth investigation, both theoretically and in practical applications.

Table 6: Iteration counts and computing time for the two-grid preconditioner with the prolongation operators generated by solving LSPs precisely and the pre-trained four-level U-Net, where “5-NN(RF)-MG” represents the prolongation operators derived from the four-level U-Net trained with Log-Gaussian random dataset.

Coefficient profiles	1-LSP-MG	3-LSP-MG	5-LSP-MG	5-NN(RF)-MG
RB $\kappa_b = 10^2$	67 (11.62)	29 (8.85)	17 (7.08)	20 (3.97)
RB $\kappa_b = 10^{-2}$	68 (11.70)	24 (7.76)	16 (7.13)	18 (3.68)
RB $\kappa_b = 10^3$	72 (12.88)	29 (9.11)	19 (7.40)	22 (4.34)
RB $\kappa_b = 10^{-3}$	71 (12.11)	24 (8.03)	17 (7.16)	20 (4.05)
RB $\kappa_b = 10^4$	77 (13.41)	30 (8.90)	19 (7.74)	25 (5.08)
RB $\kappa_b = 10^{-4}$	82 (14.43)	27 (8.19)	17 (7.45)	22 (4.52)
RB $\kappa_b = 10^5$	136 (23.40)	34 (9.76)	21 (8.00)	28 (5.47)
RB $\kappa_b = 10^{-5}$	121 (21.06)	29 (9.13)	20 (7.85)	26 (5.18)

5 Conclusion and future work

This research addressed the computational challenges of linear systems from Darcy flow discretization under random permeability. Traditional generalized multiscale two-grid methods require solving a local spectral problem for each coarse element, which was time-consuming, while its robustness on the high-contrast coefficient are guaranteed. We proposed a deep learning based surrogate model using a four-level U-Net to generate blocks of the generalized multiscale prolongation operator directly from coarse element coefficients. Our loss function was based on the distance between subspaces defined by these coefficients. We achieved a label generation time reduction of up to 5 folds through symmetric transformations and enhanced data efficiency via Karhunen–Loève expansion. Numerical experiments showed that our method reduced prolongation operator generation time by up to a factor of 5 while preserving the efficiency of the two-grid preconditioner. For the generalization ability of neural networks, our trained model is applicable to different sizes of coarse element. Besides, the model trained on low-contrast datasets remains significantly effective when applied to high-contrast and off-distribution cases. Recognizing the mutual influence of the smoother and the prolongation operator is essential for enhancing the effectiveness of the two-grid preconditioner. Our future work will focus on developing an optimal smoother by deep learning to further enhance preconditioning.

Acknowledgments

During the edition of this work, the authors utilized ChatGPT to enhance readability and language quality. Following the use of this tool, the authors thoroughly reviewed and as needed and accept full responsibility for the final publication.

References

- [1] J. E. AARNES, *On the use of a mixed multiscale finite element method for greater flexibility and increased speed or improved accuracy in reservoir simulation*, Multiscale Modeling & Simulation, 2 (2004), pp. 421–439.
- [2] P. F. ANTONIETTI AND G. PENNESI, *V-cycle multigrid algorithms for discontinuous galerkin methods on non-nested polytopic meshes*, Journal of Scientific Computing, 78 (2019), pp. 625–652.

- [3] T. ARBOGAST, G. PENCHEVA, M. F. WHEELER, AND I. YOTOV, *A multiscale mortar mixed finite element method*, Multiscale Modeling & Simulation, 6 (2007), pp. 319–346.
- [4] T. ARBOGAST AND H. XIAO, *A multiscale mortar mixed space based on homogenization for heterogeneous elliptic problems*, SIAM Journal on Numerical Analysis, 51 (2013), pp. 377–399.
- [5] J. BEAR AND A. H.-D. CHENG, *Modeling groundwater flow and contaminant transport*, vol. 23, Springer, 2010.
- [6] N. BELL, L. OLSON, AND J. SCHRODER, *PyAMG: Algebraic multigrid solvers in python*, Journal of Open Source Software, 7 (2022), p. 4142.
- [7] D. BOFFI, F. BREZZI, AND M. FORTIN, *Mixed Finite Element Methods and Applications*, vol. 44, Springer, 2013.
- [8] A. BRANDT, S. MACCORMICK, AND J. RUGE, *Algebraic multigrid (AMG) for automatic multigrid solution with application to geodetic computations*, 1983.
- [9] T. CHEN AND H. CHEN, *Universal approximation to nonlinear operators by neural networks with arbitrary activation functions and its application to dynamical systems*, IEEE transactions on neural networks, 6 (1995), pp. 911–917.
- [10] Z. CHEN, W. DENG, AND H. YE, *Upscaling of a class of nonlinear parabolic equations for the flow transport in heterogeneous porous media*, Communications in Mathematical Sciences, 3 (2005), pp. 493–515.
- [11] Z. CHEN AND T. HOU, *A mixed multiscale finite element method for elliptic problems with oscillating coefficients*, Mathematics of computation, 72 (2003), pp. 541–576.
- [12] E. T. CHUNG, Y. EFENDIEV, AND T. Y. HOU, *Multiscale Model Reduction*, Springer, 2023.
- [13] E. T. CHUNG, Y. EFENDIEV, AND C. S. LEE, *Mixed generalized multiscale finite element methods and applications*, Multiscale Modeling & Simulation, 13 (2015), pp. 338–366.
- [14] N. R. COUNCIL, D. ON EARTH, L. STUDIES, C. ON GEOSCIENCES, C. ON FRACTURE CHARACTERIZATION, AND F. FLOW, *Rock fractures and fluid flow: contemporary understanding and applications*, National Academies Press, 1996.
- [15] L. J. DURLOFSKY, *Numerical calculation of equivalent grid block permeability tensors for heterogeneous porous media*, Water resources research, 27 (1991), pp. 699–708.
- [16] Y. EFENDIEV, J. GALVIS, AND T. Y. HOU, *Generalized multiscale finite element methods (gmsfem)*, Journal of computational physics, 251 (2013), pp. 116–135.
- [17] D. GREENFELD, M. GALUN, R. BASRI, I. YAVNEH, AND R. KIMMEL, *Learning to optimize multigrid PDE solvers*, in International Conference on Machine Learning, PMLR, 2019, pp. 2415–2423.
- [18] H. HAJIBEYGI AND P. JENNY, *Multiscale finite-volume method for parabolic problems arising from compressible multiphase flow in porous media*, Journal of Computational Physics, 228 (2009), pp. 5129–5147.
- [19] T. Y. HOU AND X.-H. WU, *A multiscale finite element method for elliptic problems in composite materials and porous media*, Journal of computational physics, 134 (1997), pp. 169–189.
- [20] A. KATRUTSA, T. DAULBAEV, AND I. OSELEDETS, *Deep multigrid: learning prolongation and restriction matrices*, arXiv preprint arXiv:1711.03825, (2017).

- [21] A. KIRILLOV, K. HE, R. GIRSHICK, C. ROTHER, AND P. DOLLÁR, *Panoptic segmentation*, 2019, <https://arxiv.org/abs/1801.00868>.
- [22] G. KUTYNIOK, P. PETERSEN, M. RASLAN, AND R. SCHNEIDER, *A theoretical analysis of deep neural networks and parametric pdes*, *Constructive Approximation*, 55 (2022), pp. 73–125.
- [23] L. LU, P. JIN, G. PANG, Z. ZHANG, AND G. E. KARNIADAKIS, *Learning nonlinear operators via DeepONet based on the universal approximation theorem of operators*, *Nature machine intelligence*, 3 (2021), pp. 218–229.
- [24] L. LU, X. MENG, Z. MAO, AND G. E. KARNIADAKIS, *DeepXDE: A deep learning library for solving differential equations*, *SIAM review*, 63 (2021), pp. 208–228.
- [25] I. LUNATI AND P. JENNY, *Multiscale finite-volume method for compressible multiphase flow in porous media*, *Journal of Computational Physics*, 216 (2006), pp. 616–636.
- [26] I. LUZ, M. GALUN, H. MARON, R. BASRI, AND I. YAVNEH, *Learning algebraic multigrid using graph neural networks*, in *International Conference on Machine Learning*, PMLR, 2020, pp. 6489–6499.
- [27] O. RONNEBERGER, P. FISCHER, AND T. BROX, *U-net: Convolutional networks for biomedical image segmentation*, in *Medical image computing and computer-assisted intervention–MICCAI 2015: 18th international conference, Munich, Germany, October 5–9, 2015, proceedings, part III 18*, Springer, 2015, pp. 234–241.
- [28] J. SCHMITT, S. KUCKUK, AND H. KÖSTLER, *Optimizing geometric multigrid methods with evolutionary computation*, arXiv preprint arXiv:1910.02749, (2019).
- [29] M. WANG, S. W. CHEUNG, E. T. CHUNG, Y. EFENDIEV, W. T. LEUNG, AND Y. WANG, *Prediction of discretization of gmsfem using deep learning*, *Mathematics*, 7 (2019), p. 412.
- [30] M. WANG, S. W. CHEUNG, W. T. LEUNG, E. T. CHUNG, Y. EFENDIEV, AND M. WHEELER, *Reduced-order deep learning for flow dynamics. the interplay between deep learning and model reduction*, *Journal of Computational Physics*, 401 (2020), p. 108939.
- [31] X.-H. WU, Y. EFENDIEV, AND T. Y. HOU, *Analysis of upscaling absolute permeability*, *Discrete and Continuous Dynamical Systems Series B*, 2 (2002), pp. 185–204.
- [32] J. XU AND L. ZIKATANOV, *Algebraic multigrid methods*, *Acta Numerica*, 26 (2017), pp. 591–721.
- [33] C. YE, S. FU, AND E. T. CHUNG, *A fast cosine transformation accelerated method for predicting effective thermal conductivity*, *Computer Methods in Applied Mechanics and Engineering*, 426 (2024), p. 116982.
- [34] C. YE, S. FU, E. T. CHUNG, AND J. HUANG, *A highly parallelized multiscale preconditioner for darcy flow in high-contrast media*, *Journal of Computational Physics*, (2024), p. 113603.
- [35] C. YE, S. FU, E. T. CHUNG, AND J. HUANG, *A robust two-level overlapping preconditioner for darcy flow in high-contrast media*, *SIAM Journal on Scientific Computing*, 46 (2024), pp. A3151–A3176.
- [36] R. W. ZIMMERMAN AND G. S. BODVARSSON, *Hydraulic conductivity of rock fractures*, *Transport in porous media*, 23 (1996), pp. 1–30.